Picosecond Lifetimes with High Quantum Yields from Single-Photon-Emitting Colloidal Nanostructures at Room Temperature

Sébastien Bidault, Alexis Devilez, Vincent Maillard, Laurent Lermusiaux, Jean-Michel Guigner, Nicolas Bonod, Jérôme Wenger

Picosecond Lifetimes with High Quantum Yields from Single-Photon Emitting Colloidal Nanostructures at Room Temperature

Sébastien Bidault,[1*] Alexis Devilez,[2] Vincent Maillard,[1] Laurent Lermusiaux,[1] Jean-Michel Guigner,[3] Nicolas Bonod[2] and Jérôme Wenger[2]

[1]*ESPCI Paris, PSL Research University, CNRS, INSERM, Institut Langevin, 1 rue Jussieu, F-75005 Paris, France*

[2]*CNRS, Aix-Marseille Université, Centrale Marseille, Institut Fresnel, UMR 7249, 13013 Marseille, France*

[3]*Institut de Minéralogie, de Physique des Matériaux, et de Cosmochimie (IMPMC), Sorbonne Universités, UMR 7590, CNRS, MNHN, Univ Paris 06, IRD UMR 206, Paris, France*

[*]*e-mail: sebastien.bidault@espci.fr*

Table of contents graphic

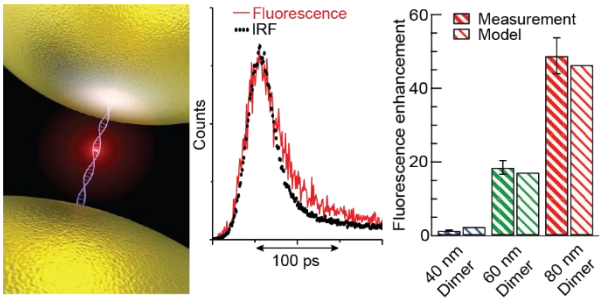

Abstract

Minimizing the luminescence lifetime while maintaining a high emission quantum yield is paramount in optimizing the excitation cross-section, radiative decay rate and brightness of quantum solid-state light sources, particularly at room temperature where non-radiative processes can dominate. We demonstrate here that DNA-templated 60 nm and 80 nm diameter gold nanoparticle dimers, featuring one fluorescent molecule, provide single-photon emission with lifetimes that can fall below 10 ps and typical quantum yields in a 45 % - 70 % range. Since these colloidal nanostructures are obtained as a purified aqueous suspension, fluorescence spectroscopy can be performed both on fixed and freely diffusing nanostructures to quantitatively estimate the distributions of decay rate and fluorescence intensity enhancements. These data are in excellent agreement with theoretical calculations and demonstrate that millions of bright fluorescent nanostructures, with radiative lifetimes below 100 ps, can be produced in parallel.

Keywords: Self-assembled nanostructures, plasmon-enhanced fluorescence, single-photon emission, fluorescence correlation spectroscopy, darkfield microscopy.

The ability of a solid-state system to absorb or emit light can be enhanced by either delocalizing its electronic wavefunction in space[1-3] or by coupling it to an optical resonator such as a dielectric cavity[4-8] or an optical antenna.[9-16] As such, semiconductor quantum wells[1] and nanoplatelets[2] or molecular light-harvesting complexes and J-aggregates[3] typically feature larger radiative decay rates and excitation cross-sections than quantum dots or organic dyes but lose the single photon-emitting properties of isolated quantum light sources. On the other hand, the efficient interaction of a quantum emitter to an optical resonator requires complex

lithography[6, 7, 17] and/or assembly strategies,[12, 13, 18] impeding the scalability of the fabrication process and limiting the study of these coupled systems to single-nanostructure measurements. The DNA-driven assembly of gold nanoparticles (AuNPs), associated with biochemical purification techniques such as electrophoresis, have recently allowed the large-scale synthesis of purified suspensions of optical antennas coupled preferentially to a single fluorescent molecule.[19, 20] However, these results have been limited to dimers of particles smaller than 40 nm in diameter that quench the quantum yield of emitters, leading to high decay rate enhancements but a weak increase of the fluorescence intensity.[21] On the contrary, assemblies of particles larger than 40 nm have been shown to strongly enhance both the decay rate and fluorescence intensity of dye molecules but their low concentration and purity have prevented the full analysis of their photophysical properties and restricted their applicability to isolated structures that are fixed on a substrate.[12, 18]

In this study, we describe the synthesis of purified suspensions of 60 nm and 80 nm diameter AuNP dimers linked preferentially by a single 10 nm long DNA double strand exhibiting one ATTO647N molecule in its center. A conjunction of ensemble and single-nanostructure spectroscopies, associated with electrodynamics calculations, allows us to characterize the brightness, decay rate and quantum yield of these systems but also the morphology, purity and plasmonic properties of the bare optical antennas. In practice, these colloidal nanostructures behave as single photon emitters with average fluorescence lifetimes of the order of 50 ps and quantum yields reaching 70 %, along with an average ×45 fluorescence intensity enhancement compared to the isolated dye that features a ϕ_0 = 65 % initial quantum yield, in excellent agreement with Mie theory estimations. These values are on par with lithographically fabricated quantum dots coupled to dielectric cavities[8] that require both cryogenic temperatures and fabrication techniques that are not currently scalable. Furthermore, we discuss how the distribution of geometrical parameters of the assembly (AuNP size, shape and spacing as well

as the emitter orientation in the dimer) leads to a significant dispersion of fluorescence intensity enhancements (up to ×330) and lifetime reductions (down to below 10 ps, at the resolution limit of our experimental setup). These single-photon sources feature some of the shortest luminescence lifetimes ever reported for single emitters[11, 16, 22] while maintaining high quantum yields as well as a scalable and reproducible fabrication procedure.

Results and discussion

Nanostructure assembly and characterization. Figure 1-a summarizes the three considered nanostructure geometries: dimers of gold nanoparticles, with diameters of 40 nm, 60 nm or 80 nm, linked by the same 30 base-pair long DNA double-strand (corresponding to a 14 nm gap, as discussed later) that features a single ATTO647N molecule in its center. These assemblies can be either used as a purified suspension or as isolated objects fixed on a Neutravidin-coated glass-slide because only one gold particle features biotin moieties on its ligand shell.[19, 23] In general, to ensure that the dimers feature only one dye molecule, gold particles functionalized with one thiolated DNA single-strand are separated from unreacted AuNPs or multilabeled nanoparticles by high-performance liquid chromatography (HPLC)[24, 25] or agarose-gel electrophoresis.[26, 27] However, these purification procedures are only compatible with up to 30 nm[25] and 40 nm gold particles,[27] respectively. We recently demonstrated the electrophoretic separation of 40 nm AuNP dimers linked preferentially by a single DNA double-strand, by minimizing the number of trithiolated DNA single-strands attached per particle.[28] In that case, most AuNPs stay unlabeled and only a few percent of the particles assemble as dimers. This percentage does not change when increasing the incubation time by a factor of 10 but is strongly modified (with a large amount of assembled AuNP trimers) when the DNA concentration is only multiplied by 2. This shows that the dimer assembly is controlled by the number of attached DNA strands and not by reaction kinetics.

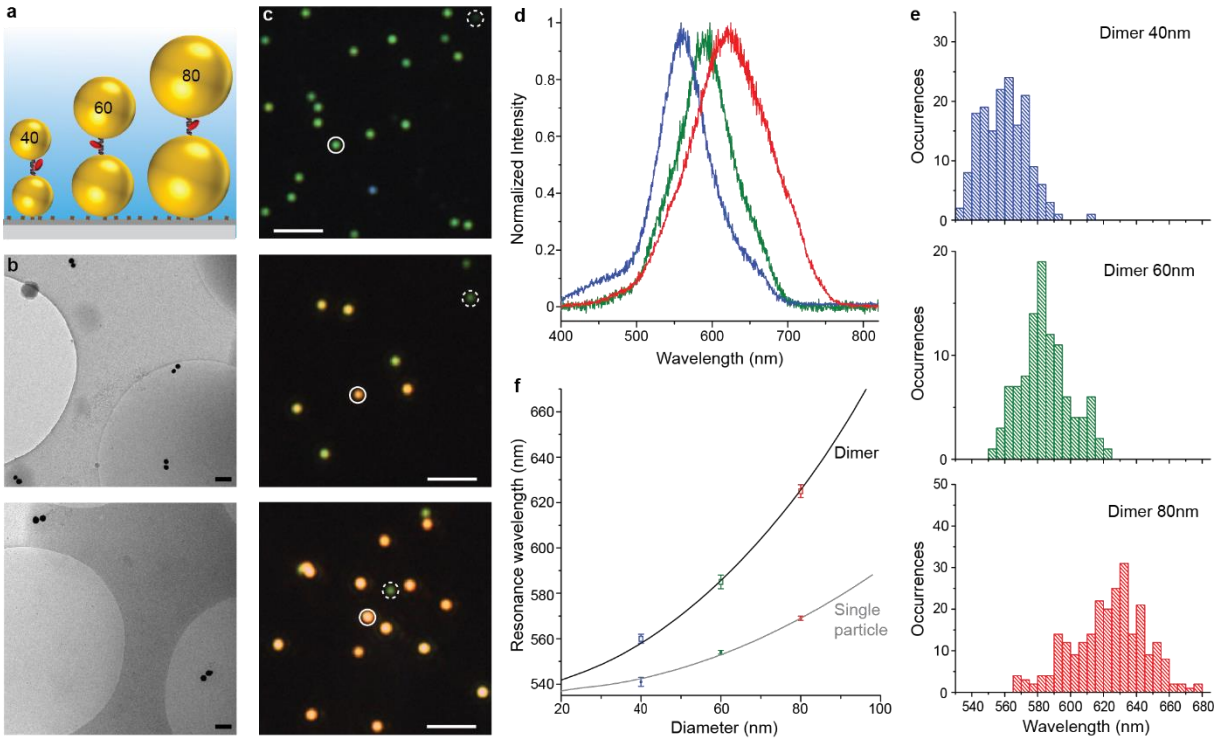

Figure 1: Gold nanoparticle dimer characterization. (a) Schematic representation of the three considered DNA-templated AuNP dimers featuring one fluorescent emitter, in solution, with one biotin-functionalized particle fixed on a Neutravidin-coated glass slide. (b) Typical cryo-electron microscopy images of 60 nm (top) and 80 nm (bottom) diameter AuNP dimers linked by a 30 bp DNA strand. Bar is 200 nm. (c) Darkfield images of 40 nm (top), 60 nm (middle) and 80 nm (bottom) gold particle dimers. The typical scattering response of a dimer is highlighted by a solid white circle while a leftover single particle is shown in a striped white circle. Bar is 5 μm. (d) Typical darkfield spectra of isolated 40 nm (blue), 60 nm (green) and 80 nm (red) AuNP dimers. (e) Distributions of plasmon resonance wavelengths for DNA-linked dimers for 40 nm (top, blue), 60 nm (middle, green) and 80 nm (bottom, red) particles. (f) Evolution of the average plasmon resonance wavelength for single particles (solid circles) and dimers (open squares) when increasing the nanoparticle size compared to Mie theory calculations for isolated gold particles (solid grey line) or pairs with a 14 nm gap (solid black line). Error bars correspond to the standard error in estimating the mean values.

As detailed in the Methods section and the Supporting Information (SI), we extend this approach to 60 nm and 80 nm AuNPs. By optimizing the DNA concentration, the local ionic strength and the electrophoretic purification, we separate dimers preferentially linked by a single DNA double-strand. In particular, Fig. S1 shows how introducing low concentrations of complementary thiolated DNA strands on the AuNPs leads to the appearance of an extra band during agarose-gel electrophoresis that, as shown on the cryo-electron microscopy images of Fig. 1-b and S2, corresponds to 60 nm and 80 nm dimers. For all particle sizes, the gold surface is passivated by ethylene glycol oligomers with only one AuNP (labelled with the DNA strand that does not feature the dye molecule) exhibiting biotin molecules.[23, 27] This ensures that, when fixing the AuNP assemblies on a Neutravidin-coated glass slide, single particles that can bind to the surface will not feature a dye-molecule.[19]

Low nanostructure concentrations in cryo-electron microscopy samples make this technique ill-suited to estimate the purity of the dimer suspensions (see Fig. S2). On the other hand, single AuNP dimers are readily imaged in darkfield microscopy and can be easily distinguished from leftover single particles and larger aggregates.[23, 27-29] For 40 nm gold particles, this widefield differentiation is possible for interparticle distances ranging between 3 nm and 20 nm: at larger distances, the response of a dimer is spectrally similar to single particles; while, for gaps below 3 nm, strong scattering from the transverse mode of the dimer requires additional polarization-dependent measurements.[28] The interparticle distance range in which the discrimination of dimers in darkfield microscopy is possible for larger particles can be readily estimated by considering that plasmon coupling scales as the ratio between the interparticle gap and the AuNP diameter, for all particle sizes.[30] In practice, Fig. 1-c shows that dimers linked by a 30 bp DNA double-strand feature scattering signals (highlighted in a solid white circle) that are both significantly stronger and red-shifted with respect to single AuNPs (striped white circle).

On a typical large scale darkfield image, up to one hundred scatterers can be compared in parallel, indicating dimer purities ranging between 75 % and 90 % for 40 nm and 60 nm AuNPs and between 60 % and 75 % for 80 nm particles, the rest being single particles with typically less than 5 % larger aggregates (see Fig. S3 and S4 for large-scale darkfield images of 60 nm and 80 nm dimers, respectively).

Darkfield microscopy also allows a measurement of the distribution of plasmon resonance wavelengths from isolated dimers and, by comparing these values to theoretical calculations, an estimation of the interparticle distance.[27, 28, 31, 32] Figure 1-d provides typical scattering spectra from 40 nm, 60 nm and 80 nm AuNP dimers, demonstrating both a spectral redshift and a reduced resonance quality factor for larger particles, as expected when increasing radiation damping in an optical antenna[33] and increasing plasmon coupling[27, 31] (as the length of the DNA linker is unchanged). Because of an unpolarized excitation, these spectra are dominated by the longitudinal mode of the dimer:[27, 28, 31] the data of Fig. 1-d do not feature a visible second peak that could be attributed to the transverse mode of the dimer. The distributions of plasmon resonance wavelengths for AuNP dimers are given in Fig. 1-e for the three particle sizes. They are strongly red-shifted with respect to the distributions for single gold particles of the same diameter (see Figure S5), further confirming the assembly of AuNP dimers. We observe a broadening of the resonance wavelength distributions for larger particles, which is due to variations in the interparticle distances as well as the AuNP sizes and shapes[27, 31] that influence more the longitudinal resonance when the plasmon coupling increases.

To estimate the interparticle distance in the different samples, we plot the mean plasmon resonance wavelengths as a function of the particle diameter on Fig. 1-e, in comparison to Mie theory calculations. These calculations use a bulk refractive index for gold[34] and a n=1.4 dielectric index for the environment, as already discussed for 40 nm AuNP dimers.[19, 27] The excellent agreement between the experimental single particle resonance wavelengths and the

theoretical values further validates these approximations for the refractive indexes. The only free parameter to estimate the theoretical diameter dependence of the longitudinal plasmon resonance of dimers is the interparticle distance. We find a quantitative agreement between Mie theory calculations and experimental values for an interparticle gap of 14 nm. This value is in excellent agreement with the 12-13 nm distance found previously with 40 nm particles linked by the same DNA sequence, for which a standard deviation of ± 2 nm for the interparticle gap was estimated from cryo-EM images and fluorescence lifetime measurements.[19, 27] The 14 nm interparticle distance corresponds to the sum of the length of the DNA molecule (10 nm) with the lengths of the trithiolated modifications used to graft DNA on the AuNP surface. The dimers are thus fully stretched by repulsive electrostatic interactions between the negatively charged particles, as expected for experiments performed at low ionic strength.[27, 28, 35] In the case of 40 nm AuNPs, this hypothesis remains valid for NaCl concentrations lower than 50 mM.[28, 35] In the present study, all optical measurements are performed with salt concentrations lower than 5 mM (see Methods).

Analysis of fluorescence intensity enhancements on freely diffusing emitters. The interaction between the single ATTO647N dye and the AuNP dimer is studied using fluorescence spectroscopy of freely diffusing or fixed nanostructures. Single nanostructure measurements on fixed emitters can readily provide decay rate estimations and photon statistics but are ill-suited to estimate absolute fluorescence intensities as the collection efficiency strongly depends on the emitter / dimer orientation with respect to the excitation direction.[11, 19] On the contrary, confocal fluorescence measurements on moving emitters average these orientation dependencies to recover quantitative light intensities.[21, 36-38] However, since the acquisition time is limited by the translational diffusion time of the emitters, not enough photons are collected to estimate single nanostructure decay rates and emission statistics.

Figure 2-a summarizes the diffusion properties of DNA-templated AuNP dimers estimated from a second order correlation of the fluorescence time-traces for freely moving nanostructures, emitting around 670 nm after excitation with a 633 nm continuous-wave laser, as shown on Fig. 2-b. The fluorescence correlation spectroscopy (FCS) analysis indicates translational diffusion times of 9.5, 16 and 20 ms for dimers of 40, 60 and 80 nm, respectively. This corresponds to hydrodynamic radii of 25, 40 and 50 nm which increase as expected for larger nanoparticle diameters. Moreover, the FCS data shows the appearance of a supplementary sub-ms correlation term corresponding to the dimer rotational diffusion time with respect to the excitation polarization.[21] For dimers of 40, 60 nm and 80 nm diameter AuNPs, the rotational diffusion times are 40, 100 and 200 μs, respectively, in good agreement with the rotational diffusion times calculated for a prolate ellipsoid following Perrin theory.[39] Altogether, these measurements confirm the high purity of the colloidal emitters and their correspondence with dimers of 40, 60 and 80 nm diameter particles.

The translational and rotational diffusion times are clearly visible in a typical fluorescence intensity time-trace, as shown on Fig. 2-c-g for 80 nm dimers. The correlation curves of Fig. 2-b, before normalization, demonstrate that the average number of emitters in the confocal detection volume is typically around 0.2. This means that the peaks of Fig. 2-c correspond to single freely moving emitters. Furthermore, we clearly observe, in Fig. 2-d-g, intensity fluctuations for a single nanostructure at sub-millisecond timescales. In particular, the photon count varies between 0 and several hundred counts per ms, showing the strong dependence of the fluorescence intensity on the relative orientation of the dimer with respect to the excitation polarization. This is due to the fluorescence intensity being maximum when the polarization is along the dimer axis (bright longitudinal mode) or essentially zero when exciting the dark transverse modes.[18]

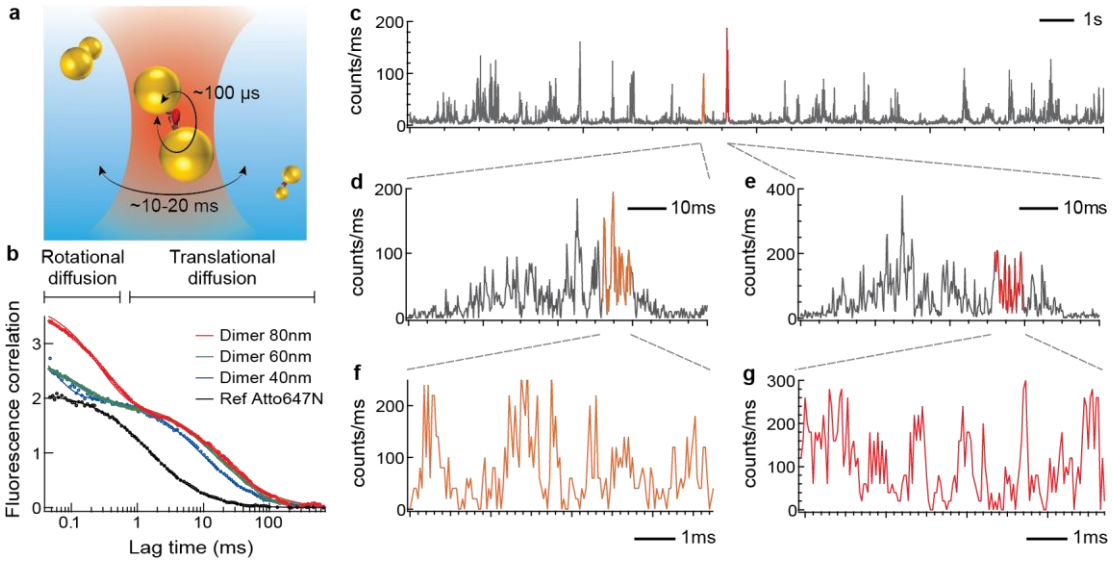

Figure 2: Fluorescence measurements on freely moving nanostructures. (a) Diffusion properties of freely moving AuNP dimers in a water suspension. (b) Amplitude-normalized FCS correlation functions for the dimer antennas and the reference Atto647N-DNA sample. As the nanoparticle diameter grows, both the rotational (sub-ms) and the translational (> 10 ms) diffusion times increase. (c-g) Fluorescence intensity time traces for 80 nm AuNP dimers diffusing in solution (excitation intensity of 1.75 kW.cm^{-2}). The individual pulses in (c) correspond to single dimers crossing the confocal detection volume. Observations within the duration of a single pulse (d-g) show sub-ms fluctuations that are representative of the dimer rotation relative to the linear excitation polarization. Binning times are 2 ms for (c), 200 µs for (d,e) and 50 µs for (f,g). All intensities are computed in counts per ms.

When using a 40 ms integration time in the fluorescence time-traces, the rotational orientation effects are averaged out and the distributions of fluorescence count rates for isolated emitters of each considered sample can be recovered for a given excitation intensity as shown in Fig. 3-a-b. These data clearly demonstrate the large fluorescence intensity enhancements observed with 60 nm and 80 nm dimers while the typical count rates measured with 40 nm particles are similar to the reference ATTO647N sample. The average fluorescence intensities per emitter

are also estimated from the number of nanostructures recovered in the correlation curves of Fig. 2-b. The evolution of these average count rates as a function of the excitation intensity is plotted in Fig. 3-c. We observe that all samples exhibit a saturation of their emission with increasing excitation, verifying that the measured signal arises from the excitation of the ATTO647N dye and not background signal from the optical antennas. Furthermore, the background signal produced by the plasmonic antennas is estimated by studying 80 nm dimers with a DNA linker that does not feature the ATTO647N dye in the same experimental conditions, accounting for less than 1 % of the photon count rates for the same sample with the fluorescent molecule (see Fig. S7). Finally, by fitting the saturation curves, it is possible to infer the count rate enhancements, η_{fluo}, in the linear regime.

Average fluorescence intensity enhancements are plotted on Fig. 3-d for both the photon count histograms (PCH) of Fig. 3-b and FCS data of Fig. 3-c. The two analysis procedures thus provide η_{fluo} values in excellent agreement, demonstrating that measurements on freely moving emitters provide quantitative estimations of the fluorescence intensities compared to the reference ATTO647N sample. Importantly, we observe that the 60 nm and 80 nm AuNP dimers enhance, on average, the fluorescence intensity of the dye by factors of ×18 and ×45, respectively, while the 40 nm particles provide a modest 40 % count rate increase.

It is important to stress that this average enhancement is obtained with a dye that features a high initial 65 % quantum yield and that much higher values are expected with low-quantum yield emitters.[18, 36, 37] Furthermore, these are mean values and much larger enhancements can be monitored in the fluorescence time-traces of 60 nm and 80 nm dimers compared to the reference sample at the same excitation intensity, as shown on the photon count histograms of Figure 3-b. For instance, Figure S8 shows that count rates as high as 615 counts per ms are measured with 80 nm AuNP dimers at an excitation intensity where the average reference ATTO647N signal is 1.85 counts per ms, corresponding to η_{fluo} = 330. A possible figure of merit for the

fluorescence enhancement, which corrects for the influence of the initial emitter quantum yield, is $\eta_{fluo} \times \phi_0$[40] providing a maximum value of 215 for the 80 nm AuNP dimers.

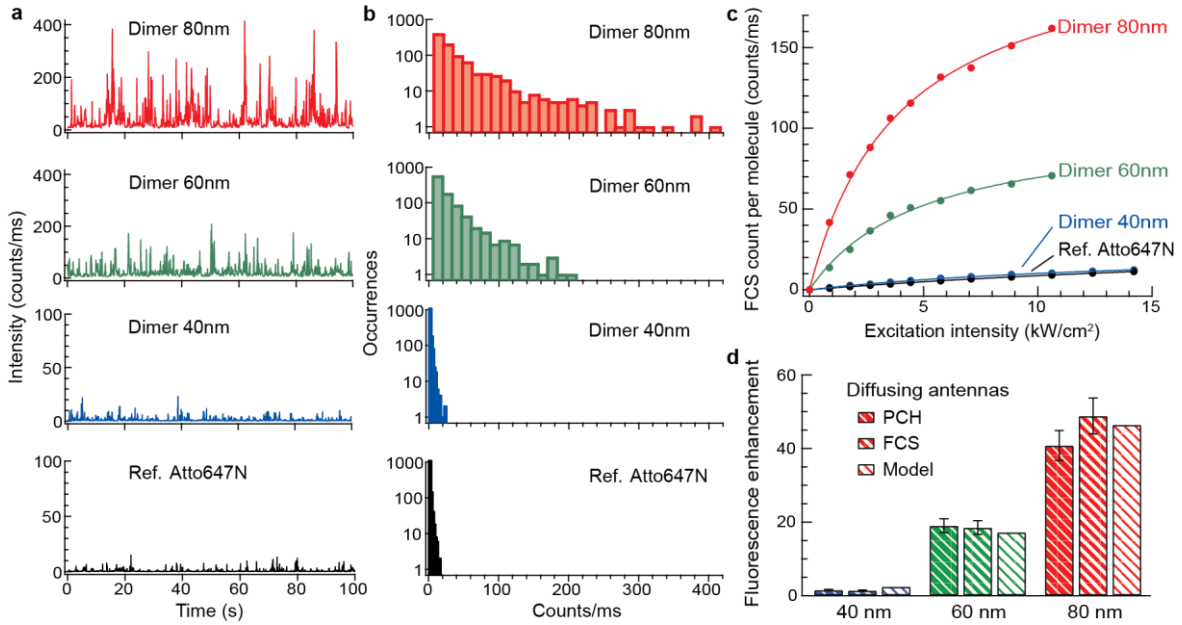

Figure 3: Average fluorescence enhancement of dimer antennas diffusing in solution. (a) Fluorescence intensity time traces for the dimer antennas of diameters 40, 60 and 80 nm and the reference Atto647N dye conjugated to double stranded DNA (3.5 kW.cm^{-2} excitation intensity at 633 nm, 40 ms binning time). (b) Fluorescence photon count histograms (PCH) deduced from the traces in (a). (c) Average fluorescence count rate per emitter measured by fluorescence correlation spectroscopy (FCS) as a function of the excitation intensity. (d) Rotational averaged fluorescence enhancement factor for dimer antennas diffusing in solution in the linear excitation regime deduced from the photon count histograms (PCH) in (b), the FCS data in (c), and orientation averaged Mie theory calculations.

Estimating theoretically the fluorescence intensity enhancement expected with DNA-templated AuNP dimers requires the knowledge of several geometrical parameters.[19] While the average interparticle distance of 14 nm is recovered from the scattering data of Fig. 1-f, the orientation

of the transition dipole of DNA-bound ATTO647N in the dimer is unknown. Furthermore, single molecule fluorescence anisotropy measurements indicate that dye molecules often feature specific orientations in DNA strands,[41, 42] while average measurements in solution demonstrate sub-ns rotational diffusion times.[43, 44] In practice, the transition dipoles of DNA-bound molecules tend to fluctuate at picosecond timescales around a preferential axis, with maximum wobbling angles ranging between a few tens of degrees to 180° (where the emission becomes unpolarized).[41]

By neglecting changes in collection efficiency as both isolated dye molecules and AuNP dimers radiate as dipoles, the increase in fluorescence count rate for the antenna system, compared to the reference ATTO647N sample, can be expressed as:[45, 46]

$$\eta_{fluo} = \frac{(I/I_0)(\Gamma_R/\Gamma_{R_0})}{1-\phi_0+\phi_0(\Gamma-\Gamma_{NR_0})/\Gamma_{R_0}}, \quad (1)$$

with Γ_{R0} and Γ_{NR0} the initial radiative and non-radiative rates of the dye molecule with $\phi_0 = \Gamma_{R0}/(\Gamma_{R0} + \Gamma_{NR0}) = \Gamma_{R0}/\Gamma_0$; Γ the total decay rate of the emitter in the antenna; and I/I_0 and Γ_R/Γ_{R0} the excitation intensity and radiative decay rate enhancements, respectively. Using Mie theory,[47] I/I_0, Γ_R/Γ_{R0}, $(\Gamma - \Gamma_{NR0})/\Gamma_{R0}$ and, thus, the total decay rate enhancement Γ/Γ_0 as well as the final effective quantum yield in the antenna, $\phi = \Gamma_R/\Gamma$, can be computed as a function of the emitter orientation for all particle sizes (see Fig. S9). These calculations show that the quantum yield, local field enhancement and, thus, the fluorescence intensity enhancement are maximum for an emitter oriented along the dimer but fall to zero when its transition dipole is oriented transversely. The theoretical average η_{fluo} values in Fig. 3-d correspond to an orientation averaged Mie theory calculation in which molecular transition dipoles are isotropically distributed in the dimer and can randomly fluctuate with a maximum 180° wobbling angle during the emission process. This model provides an excellent agreement with the experimentally measured η_{fluo} values, demonstrating that the strong increase in fluorescence

count rates when substituting 40 nm particles for 60 nm or 80 nm AuNPs is supported by classical electrodynamics calculations.

Single-photon emission and estimation of the fluorescence decay rates and quantum yields. Along with the fluorescence intensity enhancement factor $\eta_{fluo} \times \phi_0$, corrected for the emitter quantum yield, another good figure of merit to highlight how an antenna enhances the emission of a single photon source is the radiative decay rate of the coupled system. Indeed, the radiative decay rate of an isolated quantum emitter is directly related to the oscillator strength and to the dipole moment of the corresponding electronic transition.[48] Enhanced Γ_R/Γ_{R0} values and single photon emission would therefore indicate that the dye-antenna system features an increased effective transition dipole moment while remaining an isolated quantum emitter. In practice, enhanced decay rates associated with high quantum yields are necessary to produce single photon sources with optimized emission rates.[8, 16]

To recover the decay rates of DNA-templated nanostructures, we measure the luminescence lifetimes of surface-bound isolated emitters using a picosecond laser excitation at 635 nm. A low 1 $kW.cm^{-2}$ excitation intensity is used to avoid saturation effects and fast photobleaching of the dye molecules. Figures 4-a-b show typical examples for the 60 nm and 80 nm dimers with clear bleaching steps and estimated lifetimes of 45 ± 10 ps and 10 ± 5 ps, respectively. Considering the mean ATTO647N initial lifetime of 3.8 ns on a double-stranded DNA strand, these values correspond to Γ/Γ_0 = 85 and 380, respectively. Furthermore, since the fluorescence signal is divided over two identical avalanche photodiodes (APDs), the emission statistics of the single nanostructure can be analyzed and show clear photon antibunching with second order correlation values at zero time delay of 0.25 and 0.35, compared to the normalized peak heights of consecutive laser pulses, for these 60 nm and 80 nm dimers. Importantly, the data of Fig. 4-b demonstrate that bright single-photon emitters can be produced with few picoseconds

lifetimes. Zero-time delay correlations amount typically to 0.25 and 0.35 for 60 nm and 80 nm AuNP dimers, respectively (see Fig. S10). These values are presently limited by a weak background signal that increases between 60 nm and 80 nm particles as the excitation wavelength is closer to the dimer plasmon resonance.

Single emitter lifetimes are estimated by fitting the experimental data with the instrument response function (IRF) of the setup convoluted by a single-exponential decay.[11, 19] The full-width at half maximum of the IRF is 35 ± 5 ps, allowing the estimation of lifetimes down to 10 ps (as in Fig. 4-b), with data that cannot be unambiguously distinguished from the response function associated with a 5 ± 5 ps lifetime and, thus, $\Gamma/\Gamma_0 = 760$. Lifetimes estimated in the 80 nm dimer sample range from several hundred picoseconds to 5 ± 5 ps (see for instance, single nanostructure data on Fig. S11 with lifetimes of 120 ± 15 ps, 25 ± 5 ps and 5 ± 5 ps). To quantitatively recover the Γ/Γ_0 distributions for both dimer samples, the luminescence lifetime from several hundred diffraction-limited spots is recorded in scanning confocal microscopy with the only selection rule that 200 photons are collected within the 20 ms integration time to properly fit the temporal decay. These data are shown in Fig. 4-c, along with the Γ/Γ_0 distribution for 40 nm particle dimers, and indicate log-normal distributions of the luminescence lifetimes.[19]

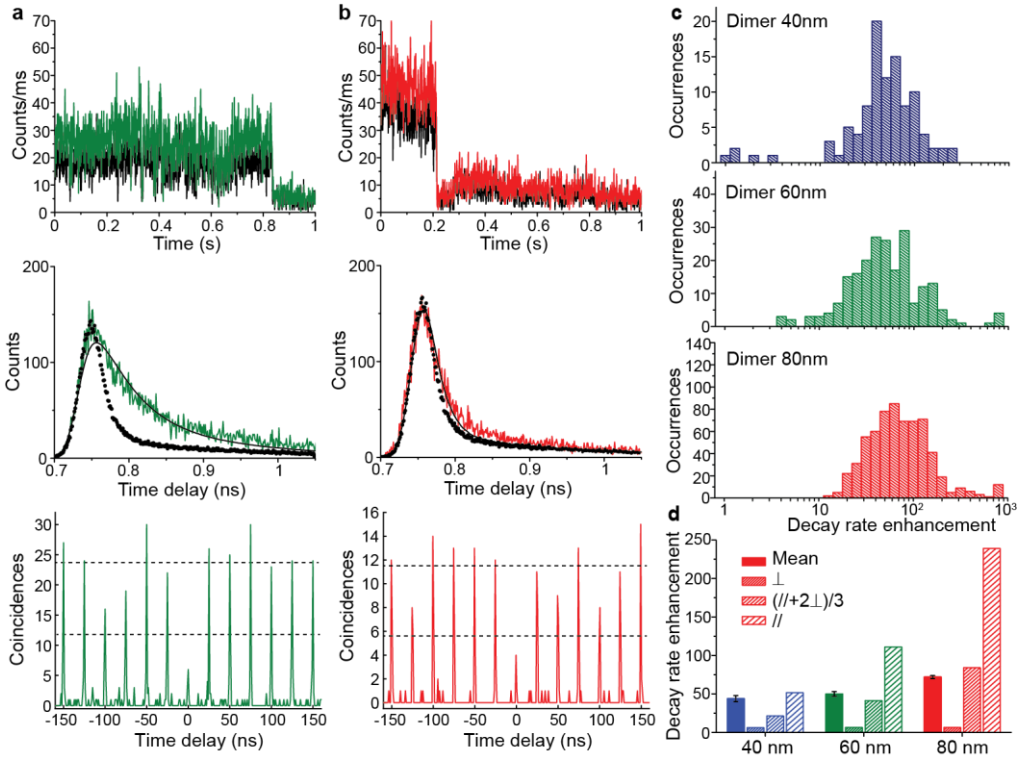

Figure 4: Fluorescence lifetime measurements and single-photon emission. Examples of fluorescence time-traces (top), lifetimes (center) and photon emission statistics (bottom) for an isolated 60 nm (a) and 80 nm AuNP dimer featuring a single ATTO647N dye. The intensity time traces exhibit two signals (solid colored and black lines) from two APDs separated by a 50/50 beamsplitter. The temporal IRF of the setup is given as black data points and the single exponential decay fit as a black solid line. The mean values of the second order correlation peaks, and their halves, are given as dashed black lines. (c) Distributions of Γ/Γ_0 for the 40 nm (top), 60 nm (center) and 80 nm (bottom) AuNP dimers in logarithmic scale. (d) Mean decay rate enhancements compared to theoretical Γ/Γ_0 values for transverse, $\perp$, orientation-averaged, $(//+2\perp)/3$, and longitudinal, //, molecular transition dipoles. The error bars are the standard errors in estimating the mean values.

The mean experimental decay rate enhancements are provided in Fig. 4-d along with the theoretical Γ/Γ_0 values for transverse, orientation-averaged and longitudinal molecular

transition dipoles. The mean decay rate enhancements reach 44 ± 4, 50 ± 3 and 72 ± 2 when increasing the AuNP diameter from 40 nm to 60 nm and 80 nm, respectively. The widths of the total decay rate distributions are due to the dispersions of AuNP sizes and interparticle distances but also to the wobbling angles of the molecular transition dipoles that can be lower than 180° and lead to a preferential orientation. In practice, the mean Γ/Γ_0 values range between the theoretical expected values for transversely and longitudinally oriented molecules, and are in good agreement with an orientation-averaged decay rate enhancement for the 60 nm and 80 nm AuNP dimers.

To estimate the effective quantum yield of the coupled emitter-antenna system, it is necessary to infer the evolution of the radiative decay rate Γ_R/Γ_{R0}. Considering the emitter as a two-level system, the saturation curves of Fig. 3-c would provide directly the change in radiative lifetime.[21] However, the excitation of higher energy states strongly influences the saturation spectroscopy of large organic dyes[49] leading to a strong underestimation of the decay rate change, and therefore of the effective quantum yield. Alternatively, the analysis of triplet state dynamics provides additional spectroscopic data to estimate ϕ.[50] However, AuNP dimer intensity time traces do not feature significant blinking dynamics (see Fig. 4 and S11).

The Γ_R/Γ_{R0} radiative decay rate change can also be estimated by considering its relationship to the local field intensity enhancement I/I_0 because of reciprocity. If the emission and excitation wavelengths, wavevectors and polarizations are identical, then $\Gamma_R/\Gamma_{R0} = I/I_0$ and equation (1) allows the estimation of the radiative decay rate enhancement and the quantum yield.[46, 51] In the considered dye-conjugated AuNP dimer measurements, the wavevector and polarization hypotheses are valid since the measurement is performed in epifluorescence and the coupling of the antenna to the far-field is dominated by the bright longitudinal mode of the dimer. However, the Stokes shift of the emitters between a 635 nm excitation and 670 nm emission, even on the broad plasmon resonances of AuNP dimers shown in Fig. 1-d, requires a correction

factor that can be estimated by Mie theory. The calculated Stokes-shifted $[(I/I_0)/(\Gamma_R/\Gamma_{R0})]$ ratios are 1.4, 1.65 and 1.25 for 40 nm, 60 nm and 80 nm AuNPs, respectively, providing estimated final quantum yields $\phi = \Gamma_R/\Gamma$ of 15 %, 45 % and 70 % for the three particle sizes. In comparison, the calculated Mie theory values of ϕ for a 60° angle are 25 %, 50 % and 70 % for 40 nm, 60 nm and 80 nm particles, respectively (Fig. S6). This means that the average quantum yields estimated for the dye-AuNP dimer assembly are in very good agreement with theoretical values for the typical orientation of randomly distributed molecular transition dipoles in the antenna. Overall, the estimated 70 % quantum yield for 80 nm AuNP dimers, associated with typical luminescence lifetimes of 50 ps, correspond to radiative lifetimes significantly lower than 100 ps compared to nearly 6 ns for the ATTO647N dye. This demonstrates unambiguously that DNA-templated AuNP dimers act as efficient optical antennas: they strongly enhance the ability of an isolated quantum emitter to radiate energy into the far-field. While geometrical and orientational effects introduce a strong dispersion in fluorescence intensity and decay rate enhancements, the highest count rates are observed for emitters with lifetimes below 100 ps (see on Fig. S12 the evolution of the measured fluorescence count rates with respect to Γ/Γ_0 for the emitters analyzed on Fig. 4-c). This proves that a high percentage of the billion dye-featuring AuNP dimers, synthesized in parallel, exhibit high radiative decay rates and quantum yields; highlighting the benefits of DNA-programmed self-assembly for the large-scale optimization of light-matter interactions at the nanoscale. A better control of the dye-DNA binding[52] to control the orientation of the molecular transition dipole in the antenna should provide an extra order of magnitude in enhancing both the intensity and decay rate enhancements while minimizing the dispersion of photophysical properties. Furthermore, DNA templates allow the controlled positioning of several organic dyes with properly engineered intermolecular interactions[53] which, coupled to optical antennas, should feature even shorter luminescence

lifetimes to control optical coherence at room temperature[54, 55] or enhance many-body processes such as superradiance.[56]

Methods

Dimer assembly and purification. Commercial 60 nm and 80 nm diameter AuNPs (BBI, UK) are coated with a negatively charged phosphine ligand (BSPP, Strem Chemicals, USA) then rinsed and concentrated by centrifugation following published procedures for 40 nm particles.[27] DNA functionalized AuNPs are obtained by incubating 12 fmol 60 nm AuNPs (resp. 5 fmol 80 nm AuNPs) with varying amounts of a 5'-trithiolated 30 bases-long DNA single strand (Fidelity Systems, USA) in a 13 mM NaCl (resp. 10 mM NaCl), 1.5 mM BSPP solution with a final volume of 10 μL. Two complementary DNA sequences are used with only one featuring an ATTO647N modification in its center. For 60 nm AuNPs, the minimum amounts of thiolated DNA molecules are 0.2 pmol and 0.6 pmol for the dye-containing sequence and bare complementary single-strand, respectively. With 80 nm AuNPs, the DNA excesses are 5 times larger. In Fig. S1-a, the DNA excess is increased 3 times by a factor of 2 for 60 nm particles. With 80 nm AuNPs in Fig. S1-b, the DNA concentration is increased twice by a factor of 2. After an overnight incubation, the DNA-conjugated 60 nm (resp. 80 nm) particles are incubated with a $\times 2.10^6$ (resp. $\times 2.10^6$) excess of thiolated / methyl terminated ethylene glycol hexamer (Polypure, Norway) for 30 min. The particles featuring the bare complementary DNA single-strand are incubated with a 8:1 mix of the same ligand and a biotinylated / thiolated ethylene glycol hexamer (Polypure, Norway: the ligand is obtained as a disulfide which is cleaved by reacting with an excess of BSPP).[27] The 60 nm (resp. 80 nm) samples are then purified by electrophoresis in a 1 % weight (resp. 0.75 %) agarose gel using a 0.5× tris-borate EDTA running buffer (Fig. S1a-b). The passivated DNA-functionalized 60 nm (resp. 80 nm) AuNPs are cut from the gel and concentrated by centrifugation before being incubated overnight in

stoichiometric amounts in 15 mM (resp. 10 mM) NaCl. The obtained suspensions are once again purified by gel electrophoresis (0.75 % weight, Figures S1-c-d) and yield the dimer samples described in Fig. 1 that are concentrated after slow sedimentation. The ATTO647N modified 30 bases long DNA sequence is the following:
5'-trithiol-GCACGAAACCTGGACXAGATGGGAACAGCA-3' (X=atto647N on C base).

Cryo-electron microscopy. The samples are observed with a cryo transmission electron microscope. Concentrated AuNP dimer suspensions (0.1-1 nM) are deposited on holey-carbon-coated grids (QUANTIFOIL, Germany). After being blotted with filter paper, the grids are frozen by being rapidly plunged into liquid ethane and are mounted and inserted in the microscope using a nitrogen-cooled side entry (Gatan 626 DH cryoholder). Observations are carried out at a temperature of -180°C in a JEOL 2100 LaB6 cryo transmission electron microscope operating at an accelerating voltage of 200kV with a low dose system (Minimum Dose System, MDS) to protect the thin ice film from irradiation before imaging and to minimize the irradiation during image capture. Images are recorded at a magnification of 6000 on a Gatan 2k × 2k UltraScan CCD camera (US1000). Additional Cryo-EM images are provided in Fig. S2.

Scattering spectroscopy of isolated nanostructures. Home-made microfluidic chambers are prepared using freshly cleaned glass coverslips that are stacked together with two layers of melted parafilm.[27] Following published protocols,[23, 27] the glass slides are functionalized with BSA-biotin (Sigma-Aldrich, USA) and Neutravidin (Thermo-Scientific, USA) before introducing the dimer suspension at a sub-nM concentration (15 min incubation) and rinsing the chamber with 200 µL of a 5 mM Tris, 5 mM NaCl buffer solution (pH=8).

Darkfield images and spectra are measured in an inverted microscope (IX71, Olympus) coupled to a color CCD (Quicam, Roper) and to a fiber-coupled (50 μm core diameter) imaging spectrometer (Acton SP300 with Pixis 100 CCD detector, Princeton Instruments). White light from a 100 W halogen lamp is focused on the sample using an oil-immersion 1.2-1.4 NA darkfield condenser. Scattered light is collected with a 100× 0.6 NA immersion-oil objective. All colour images are obtained with a 500 ms acquisition time.

To measure several scattering spectra in parallel (typically up to 10), the center of each AuNP grouping, with respect to the equivalent position of the fiber in the sample plane, is estimated on the color CCD image. The piezoelectric stage on which the sample is placed (P562-3CD, PI) is then programmed to align successively each grouping on the confocal detection volume of the fiber in order to measure a raw spectrum with a 5 s acquisition time. A background spectrum is measured with the same acquisition time on an empty area of the sample. The background is subtracted to the measured spectra before correction according to the wavelength-dependent illumination and detection. The distributions of resonance wavelengths for single 40 nm, 60 nm and 80 nm AuNPs is given in Fig. S5.

Fluorescence measurements on freely diffusing nanostructures. The experimental setup is based on a confocal microscope equipped with a 40x 1.2NA water immersion objective (Zeiss C-Apochromat). The excitation source is a linearly polarized CW He-Ne laser operating at 633 nm. To ensure that at least 0.2 fluorescent emitters are detected in the confocal volume while the typical concentrations are about 200 pM, we underfill the microscope objective back aperture (4 mm instead of 8.9 mm) and use a 100 μm confocal pinhole conjugated to the object plane. FCS experiments on Alexa Fluor solutions calibrate the confocal volume to 4.5 fL and the transversal waist to w_{xy} = 570 nm. After the confocal pinhole, the detection is performed by two avalanche photodiodes (PicoQuant MPD-5CTC). To separate the fluorescence light from

the epi-reflected laser and elastically scattered light, we use a dichroic mirror (Omega Filters 650DRLP), a long pass filter (Omega Filters 640AELP) and a 670 ± 20 nm fluorescence bandpass filter (Omega Filters 670DF40) in front of each photodiode. Fluorescence spectra (Fig. S4) are measured by sending the emitted photons, after the confocal pinhole, to a spectrograph (Jobin-Yvon SPEX 270M) equipped with a nitrogen-cooled CCD detector. For fluorescence correlation spectroscopy (FCS), the fluorescence intensity temporal fluctuations are analyzed by cross-correlating the signal from the photodiodes with a ALV6000 hardware correlator. Each individual FCS measurement is obtained by averaging at least 20 runs of 10 s duration each. A reference measurement with 80 nm AuNP dimers that do not feature the dye molecule is given in Fig. S5 while a typical fluorescence time-trace for the 80 nm AuNP dimer sample in provided in Figure S8.

Mie theory calculations. Calculations are performed using an in-house Generalized Mie Theory code.[47] The emission wavelength is set at 670 nm and the excitation at 635 nm. The refractive index of the surrounding medium is set at 1.4 for comparison to experiments performed at inhomogeneous glass-water interfaces[19, 27] while the dielectric constant of gold is tabulated from published data.[34] Calculations are performed with 30 multipoles. The calculated total decay rate Γ/Γ_0 enhancement, final effective quantum yield ϕ and fluorescence intensity enhancement η_{fluo} (averaged over the dimer orientations with respect to a linearly polarized excitation) are given in Fig. S9.

Single-emitter fluorescence measurements. Flow chambers with fixed isolated emitters are fabricated using the same protocol as for scattering spectroscopy measurements. The sample is illuminated in an inverted microscope (Olympus IX71) using a 1.3 NA oil-immersion objective with a tunable laser source (iChrome, Toptica) that delivers 3.5 ps pulses at a 40 MHz repetition

rate, with a wavelength fixed at 635 nm and associated with a bandpass filter (Z633/10x, Chroma) and a dichroic mirror (Z633RDC, Chroma). After spectral filtering with a highpass filter (HQ665LP, Chroma), the fluorescence signal is imaged on an EMCCD camera (Ixon, Andor) or focused on two avalanche photodiodes (APDs, MPD-5CTC), separated by a 50/50 beamsplitter. Time correlated single photon counting (Hydraharp 400, Picoquant) is used to estimate the fluorescence lifetime and photon emission statistics of single fluorescent nanostructures. Antibunching measurements are performed in a Hanbury Brown and Twiss architecture using either the laser (Fig. 4-a-b) or one APD (Fig. S10) as the trigger source. Figure S11 shows examples of fluorescence time-traces and lifetimes measured with 80 nm AuNPs. The fluorescence lifetime distributions for 60 nm and 80 nm dimers (shown in Fig. 4-c) are estimated from several hundred diffraction-limited spots recorded when scanning the sample in areas of 200 μm × 200 μm. Apart from the size of the fluorescent area with respect to the wavelength, the only selection rule is that at least 200 photons are collected within the 20 ms integration time to properly fit the temporal decay. The distribution of fluorescence count rates, as a function of the estimated lifetime, for each fluorescent area is given in Fig. S12.

Acknowledgements

The authors thank D. Bouchet for help on the antibunching data analysis. This work received funding from the Agence Nationale de la Recherche via project ANR 11 BS10 002 02. Research at Institut Langevin was supported by Agence Nationale de la Recherche via project ANR 11 JS10 002 01, by LABEX WIFI (Laboratory of Excellence within the French Program "Investments for the Future") under references ANR-10-LABX-24 and ANR-10-IDEX-0001-02 PSL*, and by Region Ile-de-France in the framework of DIM Nano-K. Work at Institut Fresnel received funding from the European Commission's Seventh Framework Programme (FP7-ICT-2011-7) under grant agreements ERC StG 278242 (ExtendFRET) and the A*MIDEX

project (No. ANR-11-IDEX-0001-02) funded by the Investissements d'Avenir French Government program and managed by the French National Research Agency (ANR).

Supporting information

Electrophoretic purification of dimers, complementary optical measurements, Mie theory calculations. This material is available free of charge *via* the Internet at http://pubs.acs.org.

References

1. Deveaud, B.; Clerot, F.; Roy, N.; Satzke, K.; Sermage, B.; Katzer, D. S. Enhanced Radiative Recombination of Free-Excitons in Gaas Quantum-Wells. *Phys. Rev. Lett.* **1991,** 67, 2355-2358.

2. Ithurria, S.; Tessier, M. D.; Mahler, B.; Lobo, R. P. S. M.; Dubertret, B.; Efros, A. Colloidal nanoplatelets with two-dimensional electronic structure. *Nat. Mater.* **2011,** 10, 936-941.

3. Wurthner, F.; Kaiser, T. E.; Saha-Moller, C. R. J-Aggregates: From Serendipitous Discovery to Supramolecular Engineering of Functional Dye Materials. *Angew. Chem. Int. Ed.* **2011,** 50, 3376-3410.

4. Reithmaier, J. P.; Sek, G.; Loffler, A.; Hofmann, C.; Kuhn, S.; Reitzenstein, S.; Keldysh, L. V.; Kulakovskii, V. D.; Reinecke, T. L.; Forchel, A. Strong coupling in a single quantum dot-semiconductor microcavity system. *Nature* **2004,** 432, 197-200.

5. Englund, D.; Fattal, D.; Waks, E.; Solomon, G.; Zhang, B.; Nakaoka, T.; Arakawa, Y.; Yamamoto, Y.; Vuckovic, J. Controlling the spontaneous emission rate of single quantum dots in a two-dimensional photonic crystal. *Phys. Rev. Lett.* **2005,** 95, 013904.

6. Hennessy, K.; Badolato, A.; Winger, M.; Gerace, D.; Atature, M.; Gulde, S.; Falt, S.; Hu, E. L.; Imamoglu, A. Quantum nature of a strongly coupled single quantum dot-cavity system. *Nature* **2007,** 445, 896-899.

7. Dousse, A.; Lanco, L.; Suffczynski, J.; Semenova, E.; Miard, A.; Lemaitre, A.; Sagnes, I.; Roblin, C.; Bloch, J.; Senellart, P. Controlled Light-Matter Coupling for a Single Quantum Dot Embedded in a Pillar Microcavity Using Far-Field Optical Lithography. *Phys. Rev. Lett.* **2008,** 101, 267404.

8. Gazzano, O.; de Vasconcellos, S. M.; Arnold, C.; Nowak, A.; Galopin, E.; Sagnes, I.; Lanco, L.; Lemaitre, A.; Senellart, P. Bright solid-state sources of indistinguishable single photons. *Nat. Commun.* **2013,** 4, 1425.

9. Anger, P.; Bharadwaj, P.; Novotny, L. Enhancement and quenching of single-molecule fluorescence. *Phys. Rev. Lett.* **2006,** 96, 113002.

10. Kuhn, S.; Hakanson, U.; Rogobete, L.; Sandoghdar, V. Enhancement of single-molecule fluorescence using a gold nanoparticle as an optical nanoantenna. *Phys. Rev. Lett.* **2006,** 97, 017402.

11. Kinkhabwala, A.; Yu, Z.; S, F.; Avlasevich, Y.; Mullen, K.; Moerner, W. E. Large single-molecule fluorescence enhancements produced by a bowtie nanoantenna. *Nature Photon.* **2009,** 3, 654-657.

12. Acuna, G. P.; Moller, F. M.; Holzmeister, P.; Beater, S.; Lalkens, B.; Tinnefeld, P. Fluorescence Enhancement at Docking Sites of DNA-Directed Self-Assembled Nanoantennas. *Science* **2012,** 338, 506-510.

13. Curto, A. G.; Taminiau, T. H.; Volpe, G.; Kreuzer, M. P.; Quidant, R.; van Hulst, N. F. Multipolar radiation of quantum emitters with nanowire optical antennas. *Nat. Commun.* **2013,** 4, 1750.

14. Wientjes, E.; Renger, J.; Curto, A. G.; Cogdell, R.; van Hulst, N. F. Strong antenna-enhanced fluorescence of a single light-harvesting complex shows photon antibunching. *Nat. Commun.* **2014,** 5, 4236.

15. Donehue, J. E.; Wertz, E.; Talicska, C. N.; Biteen, J. S. Plasmon-Enhanced Brightness and Photostability from Single Fluorescent Proteins Coupled to Gold Nanorods. *J. Phys. Chem. C* **2014,** 118, 15027-15035.

16. Hoang, T. B.; Akselrod, G. M.; Mikkelsen, M. H. Ultrafast Room-Temperature Single Photon Emission from Quantum Dots Coupled to Plasmonic Nanocavities. *Nano Lett.* **2016,** 16, 270-275.

17. Belacel, C.; Habert, B.; Bigourdan, F.; Marquier, F.; Hugonin, J. P.; de Vasconcellos, S. M.; Lafosse, X.; Coolen, L.; Schwob, C.; Javaux, C.; Dubertret, B.; Greffet, J. J.; Senellart, P.; Maitre, A. Controlling Spontaneous Emission with Plasmonic Optical Patch Antennas. *Nano Lett.* **2013,** 13, 1516-1521.

18. Puchkova, A.; Vietz, C.; Pibiri, E.; Wünsch, B.; Sanz Paz, M.; Acuna, G. P.; Tinnefeld, P. DNA Origami Nanoantennas with over 5000-fold Fluorescence Enhancement and Single-Molecule Detection at 25 μM. *Nano Lett.* **2015,** 15, 8354-8359.

19. Busson, M. P.; Rolly, B.; Stout, B.; Bonod, N.; Bidault, S. Accelerated single photon emission from dye molecule-driven nanoantennas assembled on DNA. *Nat. Commun.* **2012,** 3, 962.

20. Pal, S.; Dutta, P.; Wang, H. N.; Deng, Z. T.; Zou, S. L.; Yan, H.; Liu, Y. Quantum Efficiency Modification of Organic Fluorophores Using Gold Nanoparticles on DNA Origami Scaffolds. *J. Phys. Chem. C* **2013,** 117, 12735-12744.

21. Busson, M. P.; Rolly, B.; Stout, B.; Bonod, N.; Wenger, J.; Bidault, S. Photonic Engineering of Hybrid Metal-Organic Chromophores. *Angew. Chem. Int. Ed.* **2012,** 51, 11083-11087.

22. Hoang, T. B.; Akselrod, G. M.; Argyropoulos, C.; Huang, J. N.; Smith, D. R.; Mikkelsen, M. H. Ultrafast spontaneous emission source using plasmonic nanoantennas. *Nat. Commun.* **2015,** 6, 7788.

23. Reinhard, B. M.; Sheikholeslami, S.; Mastroianni, A.; Alivisatos, A. P.; Liphardt, J. Use of plasmon coupling to reveal the dynamics of DNA bending and cleavage by single EcoRV restriction enzymes. *Proc. Natl. Acad. Sci. U.S.A.* **2007,** 104, 2667-2672.

24. Claridge, S. A.; Goh, S. L.; Frechet, J. M. J.; Williams, S. C.; Micheel, C. M.; Alivisatos, A. P. Directed assembly of discrete gold nanoparticle groupings using branched DNA scaffolds. *Chem. Mater.* **2005,** 17, 1628-1635.

25. Lee, S. E.; Chen, Q.; Bhat, R.; Petkiewicz, S.; Smith, J. M.; Ferry, V. E.; Correia, A. L.; Alivisatos, A. P.; Bissell, M. J. Reversible Aptamer-Au Plasmon Rulers for Secreted Single Molecules. *Nano Lett.* **2015,** 15, 4564-4570.

26. Zanchet, D.; Micheel, C. M.; Parak, W. J.; Gerion, D.; Alivisatos, A. P. Electrophoretic isolation of discrete Au nanocrystal/DNA conjugates. *Nano Lett.* **2001,** 1, 32-35.

27. Busson, M. P.; Rolly, B.; Stout, B.; Bonod, N.; Larquet, E.; Polman, A.; Bidault, S. Optical and Topological Characterization of Gold Nanoparticle Dimers Linked by a Single DNA Double Strand. *Nano Lett.* **2011,** 11, 5060-5065.

28. Lermusiaux, L.; Maillard, V.; Bidault, S. Widefield Spectral Monitoring of Nanometer Distance Changes in DNA-Templated Plasmon Rulers. *ACS Nano* **2015,** 9, 978-990.

29. Lee, Y. K.; Kim, S.; Oh, J. W.; Nam, J. M. Massively Parallel and Highly Quantitative Single-Particle Analysis on Interactions between Nanoparticles on Supported Lipid Bilayer. *J. Am. Chem. Soc.* **2014,** 136, 4081-4088.

30. Jain, P. K.; Huang, W. Y.; El-Sayed, M. A. On the universal scaling behavior of the distance decay of plasmon coupling in metal nanoparticle pairs: A plasmon ruler equation. *Nano Lett.* **2007,** 7, 2080-2088.

31. Reinhard, B. M.; Siu, M.; Agarwal, H.; Alivisatos, A. P.; Liphardt, J. Calibration of dynamic molecular rulers based on plasmon coupling between gold nanoparticles. *Nano Lett.* **2005,** 5, 2246-2252.

32. Chen, T. H.; Hong, Y.; Reinhard, B. M. Probing DNA Stiffness through Optical Fluctuation Analysis of Plasmon Rulers. *Nano Lett.* **2015,** 15, 5349-5357.

33. Sönnichsen, C.; Franzl, T.; Wilk, T.; von Plessen, G.; Feldmann, J.; Wilson, O.; Mulvaney, P. Drastic Reduction of Plasmon Damping in Gold Nanorods. *Phys. Rev. Lett.* **2002,** 88, 077402.

34. Johnson, P. B.; Christy, R. W. Optical Constants of the Noble Metals. *Phys. Rev. B* **1972,** 6, 4370-4379.

35. Lermusiaux, L.; Bidault, S. Increasing the Morphological Stability of DNA-Templated Nanostructures with Surface Hydrophobicity. *Small* **2015,** 11, 5696-5704.

36. Aouani, H.; Mahboub, O.; Bonod, N.; Devaux, E.; Popov, E.; Rigneault, H.; Ebbesen, T. W.; Wenger, J. Bright Unidirectional Fluorescence Emission of Molecules in a Nanoaperture with Plasmonic Corrugations. *Nano Lett.* **2011,** 11, 637-644.

37. Punj, D.; Mivelle, M.; Moparthi, S. B.; van Zanten, T. S.; Rigneault, H.; van Hulst, N. F.; Garcia-Parajo, M. F.; Wenger, J. A plasmonic /`antenna-in-box/' platform for enhanced single-molecule analysis at micromolar concentrations. *Nat. Nanotechnol.* **2013,** 8, 512-516.

38. Khatua, S.; Paulo, P. M. R.; Yuan, H.; Gupta, A.; Zijlstra, P.; Orrit, M. Resonant Plasmonic Enhancement of Single-Molecule Fluorescence by Individual Gold Nanorods. *ACS Nano* **2014,** 8, 4440-4449.

39. Pieper, C. M.; Enderlein, J. Fluorescence correlation spectroscopy as a tool for measuring the rotational diffusion of macromolecules. *Chem. Phys. Lett.* **2011,** 516, 1-11.

40. Gill, R.; Tian, L.; Somerville, W. R. C.; Le Ru, E. C.; van Amerongen, H.; Subramaniam, V. Silver Nanoparticle Aggregates as Highly Efficient Plasmonic Antennas for Fluorescence Enhancement. *J. Phys. Chem. C* **2012,** 116, 16687-16693.

41. Ha, T.; Glass, J.; Enderle, T.; Chemla, D. S.; Weiss, S. Hindered rotational diffusion and rotational jumps of single molecules. *Phys. Rev. Lett.* **1998,** 80, 2093-2096.

42. Busson, M. P.; Bidault, S. Selective Excitation of Single Molecules Coupled to the Bright Mode of a Plasmonic Cavity. *Nano Lett.* **2014,** 14, 284-288.

43. Di Fiori, N.; Meller, A. The Effect of Dye-Dye Interactions on the Spatial Resolution of Single-Molecule FRET Measurements in Nucleic Acids. *Biophys. J.* **2010,** 98, 2265-2272.

44. Kupstat, A.; Ritschel, T.; Kumke, M. U. Oxazine Dye-Conjugated DNA Oligonucleotides: Forster Resonance Energy Transfer in View of Molecular Dye-DNA Interactions. *Bioconjugate Chem.* **2011,** 22, 2546-2557.

45. Bharadwaj, P.; Novotny, L. Spectral dependence of single molecule fluorescence enhancement. *Opt. Express* **2007,** 15, 14266-14274.

46. Regmi, R.; Al Balushi, A. A.; Rigneault, H.; Gordon, R.; Wenger, J. Nanoscale volume confinement and fluorescence enhancement with double nanohole aperture. *Sci. Rep.* **2015,** 5, 15852.

47. Stout, B.; Devilez, A.; Rolly, B.; Bonod, N. Multipole methods for nanoantennas design: applications to Yagi-Uda configurations. *J. Opt. Soc. Am. B* **2011,** 28, 1213-1223.

48. Cohen-Tannoudji, C.; Dupont-Roc, J.; Grynberg, G., *Atom-photon interactions : basic processes and applications*. Wiley: New York, 1992.

49. Winckler, P.; Jaffiol, R. Multiphoton Cascade Absorption in Single Molecule Fluorescence Saturation Spectroscopy. *Anal. Chem.* **2013,** 85, 4735-4744.

50. Holzmeister, P.; Pibiri, E.; Schmied, J. J.; Sen, T.; Acuna, G. P.; Tinnefeld, P. Quantum yield and excitation rate of single molecules close to metallic nanostructures. *Nat. Commun.* **2014,** 5, 5356.

51. Cao, D.; Cazé, A.; Calabrese, M.; Pierrat, R.; Bardou, N.; Collin, S.; Carminati, R.; Krachmalnicoff, V.; De Wilde, Y. Mapping the Radiative and the Apparent Nonradiative Local Density of States in the Near Field of a Metallic Nanoantenna. *ACS Photonics* **2015,** 2, 189-193.

52. Lee, W.; von Hippel, P. H.; Marcus, A. H. Internally labeled Cy3/Cy5 DNA constructs show greatly enhanced photo-stability in single-molecule FRET experiments. *Nucleic Acids Res.* **2014,** 42, 5967-5977.

53. Winiger, C. B.; Langenegger, S. M.; Calzaferri, G.; Häner, R. Formation of Two Homo-chromophoric H-Aggregates in DNA-Assembled Alternating Dye Stacks. *Angew. Chem. Int. Ed.* **2015,** 54, 3643-3647.

54. Aberra Guebrou, S.; Symonds, C.; Homeyer, E.; Plenet, J. C.; Gartstein, Y. N.; Agranovich, V. M.; Bellessa, J. Coherent Emission from a Disordered Organic Semiconductor Induced by Strong Coupling with Surface Plasmons. *Phys. Rev. Lett.* **2012,** 108, 066401.

55. Vasa, P.; Wang, W.; Pomraenke, R.; Lammers, M.; Maiuri, M.; Manzoni, C.; Cerullo, G.; Lienau, C. Real-time observation of ultrafast Rabi oscillations between excitons and plasmons in metal nanostructures with J-aggregates. *Nature Photon.* **2013,** 7, 128-132.

56. Törma, P.; Barnes, W. L. Strong coupling between surface plasmon polaritons and emitters: a review. *Rep. Prog. Phys.* **2015,** 78, 013901.